JOURNAL OF SPACECRAFT AND ROCKETS
Vol. 46, No. 6, November–December 2009

Navier–Stokes Predictions of Dynamic Stability Derivatives: Evaluation of Steady-State Methods

James DeSpirito,* Sidra I. Silton,† and Paul Weinacht‡
U.S. Army Research Laboratory, Aberdeen Proving Ground, Maryland 21005

DOI: 10.2514/1.38666

The prediction of the dynamic stability derivatives, roll damping, Magnus moments, and pitch-damping moments were evaluated for three spin-stabilized projectiles using steady-state computational fluid dynamic calculations. Roll-damping computational fluid dynamic predictions were found to be very good across the Mach number range investigated. Magnus moment predictions were very good in the supersonic flight regime but the accuracy varied in the sub- and transonic flight regime. The best Magnus moment prediction in the subsonic flight regime was for the non-boat-tailed projectile that did not exhibit highly nonlinear Magnus moments. A primary contribution of this paper is the demonstration that the pitch-damping moment can be adequately predicted via steady-state methods, rather than resorting to unsteady techniques. The predicted pitch-damping moment compared very well with experimental data for the three projectiles investigated. For one configuration, the pitch-damping moment was predicted by several computational fluid dynamic codes, two different steady-state methods, and a time-accurate planar pitching motion method. All methods compared very well with each other and to the experimental data.

Nomenclature

C_{l_p}	=	roll-damping coefficient
C_m	=	pitching moment coefficient
$C_{m_q} + C_{m_{\dot{\alpha}}}$	=	pitch-damping moment coefficient sum
C_{m_α}	=	slope of pitching moment coefficient with angle of attack
C_{N_α}	=	slope of normal force coefficient with angle of attack
C_n	=	side moment coefficient
$C_{n_{p\alpha}}$	=	slope of Magnus moment coefficient with angle of attack
$C_{n_{\dot{\phi}}}$	=	slope of side moment coefficient with coning rate
d	=	missile base diameter, m
k	=	turbulence kinetic energy, m^2/s^2
M	=	Mach number
p	=	projectile spin rate, in nonrolling coordinate frame, rad/s
q_∞	=	dynamic pressure, $\frac{1}{2}\rho V^2$, N/m^2
R	=	undamped eddy viscosity, $\pi d^2/4$, m^2/s
S	=	projectile cross-sectional area, m^2
t	=	time, s
V	=	freestream velocity, m/s
x, y, z	=	axial, horizontal, and vertical body axes
x_{cg}	=	center of gravity location, cal.
x_{cp}	=	normal force center of pressure location, $x_{\text{cg}} - (C_{m_\alpha}/C_{N_\alpha})$, cal.
y^+	=	nondimensional wall distance
α	=	vertical component of angle of attack in nonrolling coordinates
$\dot{\alpha}$	=	time rate of change of angle of attack, s^{-1}
α_t	=	total angle of attack, $\sqrt{\alpha^2 + \beta^2}$
α_0	=	amplitude of angle of attack for forced planar pitching motion, rad
$\dot{\alpha}_0$	=	frequency of forced planar pitching motion, s^{-1}
β	=	horizontal component of angle of attack in nonrolling coordinates
γ	=	cosine of total angle of attack
δ	=	sine of total angle of attack
ε	=	turbulence dissipation rate, m^2/s^2
ρ	=	density, kg/m^3
$\dot{\phi}$	=	coning rate of projectile, rad/s
Ω	=	coning rate of projectile, nondimensionalized by $2V/d$
ω	=	spin rate in coning reference frame, rad/s

Presented as Paper 214 at the 46th AIAA Aerospace Sciences Meeting and Exhibit, Reno, NV, 7–10 Jan. 2008; received 1 August 2008; revision received 9 July 2009; accepted for publication 21 July 2009.

*Aerospace Engineer, Weapons and Materials Research Directorate. Associate Fellow AIAA.
†Aerospace Engineer, Weapons and Materials Research Directorate. Senior Member AIAA.
‡Aerospace Engineer, Weapons and Materials Research Directorate. Associate Fellow AIAA.

I. Introduction

COMPUTATIONAL fluid dynamic (CFD) calculations to accurately predict the static aerodynamic coefficients (e.g., drag, longitudinal, and lateral forces and moments) and flow phenomena of many geometrically complex, single and multibody projectiles, and missiles are routinely used by many investigators using commercial and government sponsored CFD software packages. The prediction of dynamic coefficients such as pitch damping, roll damping, and Magnus moment has not achieved such widespread use, even though some methods for efficient prediction via steady-state methods (e.g., for pitch damping) were demonstrated over 10 years ago [1–6]. To determine the full set of static and dynamic aerodynamic data needed to predict projectile in-flight motion, projectile designers still turn to flight tests (both aeroballistic range and telemetry free flight) as their primary source for dynamic aerodynamic coefficients. If CFD can be proven to efficiently provide accurate dynamic data, in addition to the static aerodynamic coefficients, it would be a great benefit to munition designers.

The prediction of dynamic aerodynamic coefficients is inherently more difficult than the basic static coefficients. However, with the computational resources, CFD solver techniques, and other advances available today, there are viable solutions to the problem. It is desired that the prediction methods are efficient enough (e.g., steady state rather than time-accurate methods when possible, reduced mesh sizes when possible, etc.) to limit the computation time to reasonable levels to impact the design phase of development programs. The results of recent work by many investigators on time-accurate CFD methods to predict dynamic coefficients are promising, but it can be computationally expensive in both time and computer resources [7–11]. The method of Sahu [11,12] is based on a time accurate,

coupled CFD, and rigid-body dynamics approach that is the equivalent of simulating the projectile flight through an aeroballistic spark range. Whereas this latter method is potentially the most accurate, it is very computationally intensive and the accuracy of the dynamic stability derivatives may be limited to the accuracy of those available from spark range data, because the same type of curve-fit data reduction methods are used to back out the aerodynamic coefficients.

The prediction of Magnus force and moment of spin-stabilized projectiles via steady-state CFD methods was demonstrated in the supersonic and high transonic regimes in early investigations [13–15]. However, that work was limited in scope due to computational resources. Recent work by U.S. Army Research Laboratory (ARL) investigators indicates that prediction of Magnus via steady-state methods in the subsonic and low transonic regime may not be as accurate as those in the supersonic regime, at least for some projectile base shapes [16–18]. Time-accurate CFD with advanced turbulence approaches (e.g., hybrid Reynolds-average Navier–Stokes [RANS] and Large-Eddy Simulation [LES]) showed improved Magnus predictions [17,18].

Roll-damping coefficients are usually adequately predicted via steady-state computations [16–18]. Weinacht et al. [1], Weinacht [2,3], and Weinacht and Sturek [4] showed success in predicting pitch damping of axisymmetric and finned projectiles across the Mach number range using a steady-state solution method with the projectile undergoing a coning motion.

This paper presents the results of several spin-stabilized projectiles of various calibers (cal.). The 20-mm U.S. Army–Navy Spinner Rocket (ANSR), the 25-mm M910 subcaliber projectile, and the 0.50-cal. projectile are included in this study. The steady-state pitch-damping results for the ANSR are also compared with unsteady methods. The pitch-damping prediction results from several CFD codes are compared for the ANSR. In addition, this paper hopes to demonstrate that all the dynamic stability derivatives of most spin-stabilized projectiles can be adequately predicted via steady-state CFD methods. The CFD prediction capabilities of the Magnus moment in the sub- and transonic flight regimes remain an issue and are discussed elsewhere [18,19].

II. Numerical Approach

A. U.S. Army–Navy Spinner Rocket

1. Model

The computational model of the 7-cal. (1 cal. = 20 mm) ANSR is shown in Fig. 1. The ANSR consists of a 2-cal. secant ogive followed by a 5-cal. cylindrical afterbody. Three c.g. locations were investigated, based on the available experimental data: 3.250, 4.036, and 4.818 cal. from the nose.

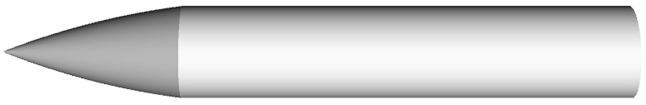

Fig. 1 ANSR model: 7 cal.

2. CFD++ Simulations

The geometry and unstructured mesh were generated using GAMBIT, a geometry and grid preprocessor supplied with the FLUENT CFD software suite [20]. A full 3-D mesh was required in all cases discussed in this paper to simulate the spinning shell at angle of attack. In generating the meshes, boundary layer mesh spacing was used near the projectile body. Resolving the viscous boundary layer is critical for predicting the Magnus and roll-damping moments; therefore, wall functions were not used, instead the option was used to integrate the equations to the wall. Normally a y^+ value on the order of 1.0 is adequate to resolve the boundary layer. However, it was desired to have a y^+ value of 0.5 or less to ensure capturing the Magnus effect of the spinning shell. All mesh stretching ratios were kept to 1.2 or less.

One mesh was generated for the Mach number range of $0.7 < M < 2.5$ and is shown in Fig. 2. An unstructured mesh consisting of 3.4×10^6hexagonal cells was used. An O-grid mesh was generated around the projectile body to contain the dense viscous mesh required to resolve the boundary layer. This O-grid extended to a distance of 0.1 cal. from the projectile body. A C-grid type mesh was then generated around the body to a distance of 0.5 cal. from the projectile body. The C-grid mesh was extended from the base of the projectile to the rear boundary of the computational domain. The region ahead of the projectile was meshed with a mapped-type mesh. The remainder of the computational domain was meshed with hexagons generated by revolving the paved quads around the axis (this is a Cooper mesh in GAMBIT). The computational domain extended for 35 cal. in front of and 50 cal. radially and behind the model. A grid resolution study performed as part of another study [19] showed that the mesh resolution was adequate. Time-accurate RANS/LES simulations were later performed [19] on the ANSR configuration using a finer mesh in the wake region. The size of that mesh was approximately 3 times the size of that used here.

The outer boundaries were set to freestream conditions at standard sea level temperature and pressure (101.325 kPa, 288 K). The projectile wall was modeled as a no-slip, isothermal (288-K) wall boundary, rotating (clockwise when viewed from rear) around the x axis at the specified spin rate. The projectile spin rates were determined from the muzzle-exit twist of 10 cal. per revolution [21], corresponding to a muzzle-exit nondimensional spin rate ($pd/2V$) of 0.315.

The commercially available CFD++ code [22], version 6.1.1, was used in this study. The CFD++ code can simulate a range of fluid dynamic phenomena, ranging from incompressible to hypersonic flow. The 3-D, time-dependent RANS equations are solved using the finite volume method. The implicit solver with dual time stepping was used. The spatial discretization was a second-order, multi-dimensional total variation diminishing (TVD) polynomial interpolation scheme. Solutions to semi-infinite Riemann problems are used in CFD++ to provide upwind flux information to the underlying transport scheme. Approximate Riemann solvers are used to determine the higher order fluxes to avoid spurious oscillations that may become physically unbounded if determined via fixed-stencil interpolation.

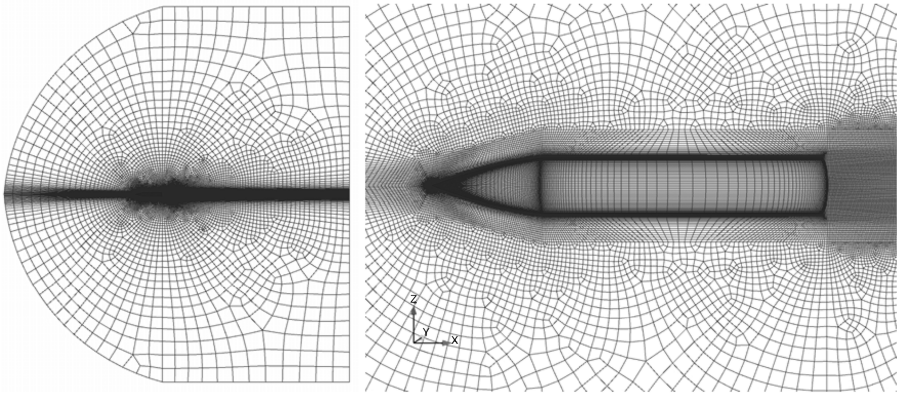

Fig. 2 Computational mesh used for 7 cal. ANSR model in CFD++ simulations.

The three-equation k–ε–R turbulence closure model, which solves transport equations for the turbulence kinetic energy, k, its dissipation rate, ε, and the undamped eddy viscosity, R, was used. This model was previously found to provide good performance across the Mach number range of interest [17]. CFD++ also has available LES models, and hybrid RANS/LES models, including the detached-eddy simulation model.

Most of the simulations were performed in parallel on an 1100-node, 4400-core, Linux Networx Advanced Technology Cluster at the U.S. ARL Major Shared Resource Center. Each node has two dual-core 3.0-GHz Intel Woodcrest processors. Some simulations were performed on an older 1024-node, Linux Networx Evolocity II system with two 3.6-GHz Intel Xeon EM64T processors per node. The number of processors used for each run was such that about 145,000–150,000 cells were partitioned on each processor. The calculations took about 11–15 s of CPU time per iteration and convergence was achieved in about 600–800 iterations. The solution was deemed converged when the flow residuals had reduced at least 3 orders of magnitude and the aerodynamic coefficients changed less than about 0.5% over the last 100 iterations. The aerodynamic coefficients were the determining factor in convergence in all cases.

The double precision solver with second-order spatial discretization was used. The maximum Courant–Friedrich–Lewy (CFL) number was chosen using the recommendations within the CFD++ solver; for example, for the transonic flow regime ($0.7 < M < 1.4$), the CFL number is ramped from 1.0 to 75.0 over the first 100 iterations.

3. Overflow 2 Simulations

The flowfield about the 7-cal. ANSR was also predicted using an overset grid approach using the NASA code Overflow 2 (OF-2)[23–25]. The method uses a near-body grid system of interconnecting grids that conform to various parts of the body surrounded by an outer, off-body Cartesian-based grid system (Fig. 3). The interconnecting near-body grids overlap and intergrid connectivity is established using a Chimera overset gridding approach. This significantly reduces the demands on grid generation of complex shapes, as each body component can be gridded independently. The outer off-body Cartesian grid system encompasses the near-body grid system and extends to the outer boundary of the computational domain. The off-body grid system typically consists of several levels of grid refinement, with the most refined grids in proximity to the near-body grids and increasingly less refined grids further away from the body.

Solution of the compressible RANS equations was accomplished using a three-factor diagonal-implicit, first-order-accurate time-stepping scheme that employs second-order accurate central differencing in space. The Baldwin and Barth [26] one-equation turbulence model was used. Characteristics based in/outflow boundary conditions have been applied on the boundaries of the domain. On the body surface, no-slip, adiabatic boundary conditions were imposed. The code was modified for use in the current study; including the addition of a tangential velocity boundary condition to account for the rigid-body rotation due to spin and the addition of the rotating coordinate frame source terms and associated outer boundary conditions required for the coning motion computations.

In addition to steady coning computations, the OF-2 code was also used to solve for pitch damping using a planar pitching motion. Typically, a simple constant-amplitude sinusoidal pitching motion is used [9,10], although other types of motion can be applied [27]. This type of computation must be performed as a time-accurate calculation because imposed motion generates an unsteady, though periodic, flowfield.

For the planar pitching motion computations, the grid motion was specified through the use of a general interface [28], which was implemented in the distributed version of the OF-2 code. This replaced the need for hard coding of the motion that had been required in earlier work using prior generations of the code. The time-dependent computations were accomplished using a body-fixed, rotating, near-body computational mesh that rotates relative to the stationary outer off-body Cartesian grid system. During the course of the investigation, it was determined that inner iterations at each time step were required to obtain a suitably converged solution. To obtain a converged solution, 5–20 inner iterations were required for the planar pitching motion computations with more inner iterations required at the trans- and subsonic velocities. Global integrated force/moment data were obtained from the computed flowfields using the FOMOCO utility [29]. Force and moment distributions along the body were also obtained from the computed flow fields through minor modifications to the existing code and additional auxiliary postprocessing tools.

The time-dependent variation of the pitching moment was computed for multiple cycles of the pitching motion. To speed the planar pitching motion computations, a nondimensional pitching rate of 0.05 was used. Computations were performed at lower pitching rates to confirm the independence of the results to angular rate. The computations were initiated from a zero-angle-of-attack steady-state solution. After about a quarter cycle of motion, the computed pitching moment displayed a periodic behavior that repeated itself with subsequent cycles of motion.

B. M910: 25-Millimeter

The M910 target-practice discarding-sabot, traced (TPDS-T) subprojectile is shown in Fig. 4. The aluminum nose consists of a 0.22-cm meplat, followed by a 4.12-cm conical ogive. The ogive is followed by a cylindrical, steel body that is 3.27-cm long with a diameter of 1.62 cm (1 cal.). A 0.2-cm chamfer forms the base of the projectile. The center of gravity is located 4.99 cm (3.08 cal.) from the nose.

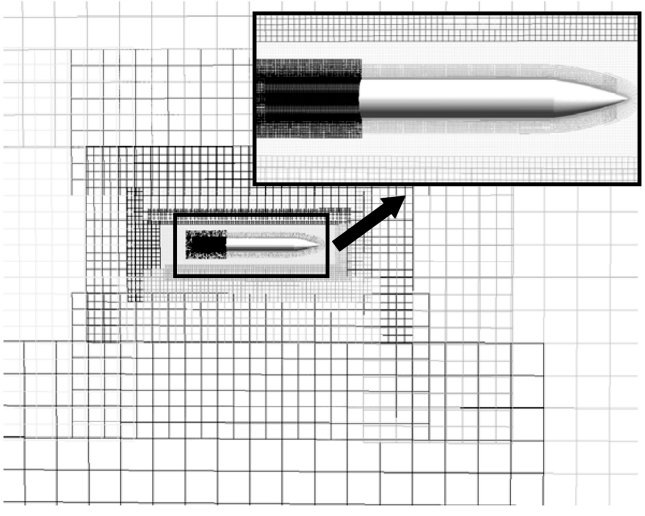

Fig. 3 Overset grids used in OF-2 ANSR computations.

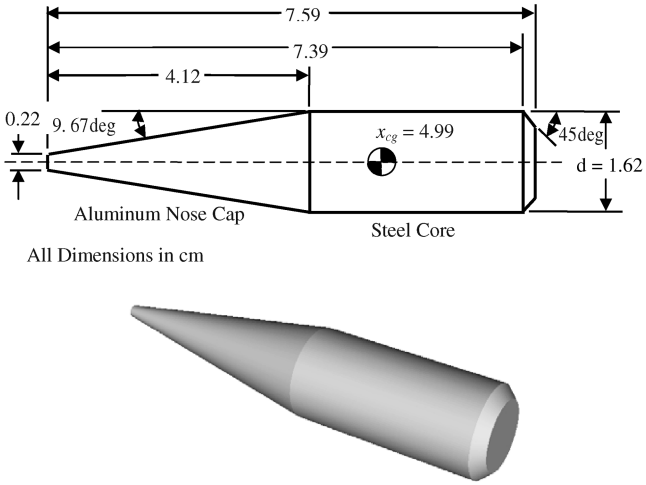

Fig. 4 Schematic and computational model of the 25-mm M910 TPDS-T subprojectile.

The geometry and unstructured mesh were generated using GAMBIT following the same methodology as for the ANSR model. Two meshes were used for the steady-state CFD calculations in this study; one for supersonic calculations ($M > 1.4$), and one for sub- and transonic calculations ($M \leq 1.4$). A grid resolution investigation performed as part of an earlier study [17] showed that the current meshes were adequate for the steady-state computations.

The properties of the meshes are compared in Table 1, including the location of the outer boundary of the computational domain with respect to the projectile. The near-body region of all meshes was similar (Fig. 5), with the sub/transonic mesh generated by making another mesh around the supersonic mesh. An O-grid was manually generated around the projectile body, building a boundary layer mesh off the entire projectile surface. The circumferential direction contained 136 cells. Also shown in Table 1 are the mesh characteristics for the time-accurate RANS/LES calculations [18]. The higher resolution mesh required in the wake region increases the total mesh size about three times that required for standard steady-state simulations.

The boundary conditions were set the same as for the ANSR model: freestream outer boundaries set to standard sea level temperature and pressure (101.325 kPa, 288 K), and no-slip, isothermal (288-K) wall boundary rotating at specified spin rate. The projectile spin rates were determined from the muzzle-exit twist of the M242 gun (23.9 cal. per revolution). The muzzle-exit nondimensional spin rate in this case is 0.131 (based on 25-mm bore diameter). CFD++ version 6.1.1 was also used in the M910 study and the solution methodology was the same as that used in the ANSR study.

C. 0.50 Caliber Projectile

The computational model of the 0.50-cal. (1 cal. = 12.95 mm) projectile is shown in Fig. 6. The projectile is 4.46 cal. long, with a 0.16-cal. long by 0.02-cal. deep groove, and a 9-deg filleted boattail. The center of gravity location is 2.68 cal. from the projectile nose. The projectile spin rates were determined from the muzzle-exit twist rate, 29.42 cal. per revolution [30], which gives the nondimensional spin rate of 0.107. The meshes used in the 0.50-cal. study were 3-D unstructured (hexahedrals, pyramids, and tetrahedrals) meshes created using GRIDGEN version 15 software [31].

Several separate meshes were constructed over the course of the original 0.50-cal. projectile study [16]. The meshes included one for subsonic and low supersonic cases, one for a near-sonic case, and two for supersonic cases. The last two grids were created to verify grid independence [16]. Two new meshes were created for the current study using the previous grids as guidance; one for supersonic flow ($M > 1.5$) and one for trans- and subsonic ($M \leq 1.5$). The properties of the two meshes, including the location of the outer boundary relative to the body, are given in Table 2. These meshes were generated with a more resolved wake region appropriate for time-accurate RANS/LES simulations and are about twice the size as those in the original 0.50-cal. study [16].

The near-body region of both meshes was similar, with the subsonic mesh generated by making another mesh around the supersonic grid. Figure 7 shows two views of the subsonic mesh; the complete subsonic mesh and a close-up showing the limits of the supersonic mesh. Each mesh contained 144 circumferential cells. An O-grid was generated around the body (0.57 cal. away) using the hyperbolic extrude feature with GRIDGEN. The grid generation characteristics, computational domain, boundary conditions, and simulation approach using CFD++ were similar to those for the ANSR and M910 studies described earlier.

III. Pitch-Damping Calculation

A. Steady Coning Methodology

The pitch-damping coefficient sum calculation follows the procedures described by Weinacht et al. [1] for axisymmetric bodies. Their approach uses a specific combination of steady-state spinning and coning motions that allows the pitch-damping force and moment coefficient to be directly related to the aerodynamic side force and moment within given constraints. The constraints are that both the coning rate and the angle of attack must be small. The flow may become unsteady at high coning rates or high angles of attack in much the same way the flow over a body at fixed angle of attack at high incidence can become unsteady due to vortex shedding. Weinacht et al. [1] use of the combined spinning and coning motion was an improvement over previous techniques that simply used a lunar coning motion (no prescribed rotation about the projectile axis) for prediction of the pitch-damping coefficients. In both cases, the projectile axis is oriented at a constant angle with respect to the freestream velocity vector, as shown in Fig. 8.

The aerodynamic side force and moment coefficients acting on a projectile in steady coning motion can be related to the pitch-damping force and moment coefficients. In steady coning motion, the longitudinal axis of the projectile performs a rotation at a constant angular velocity about a line parallel to the freestream velocity vector and coincident with the projectile center of gravity. In steady lunar coning motion, the angular velocity of the projectile results purely from the rotation, Ω, of the projectile about the freestream velocity vector. The angular velocity includes a component along the projectile's longitudinal axis, which by definition is the spin rate of the projectile in the nonrolling coordinate system [1], $p = \dot{\phi}\cos\alpha_t = \dot{\phi}\gamma$, where $\alpha_t = \sqrt{\alpha^2 + \beta^2}$. In the combined spinning and coning motion, the angular velocity of the projectile is the vector sum of two angular velocity vectors. The first vector produces a rotation of the projectile axis about the freestream velocity vector (coning motion) $\dot{\phi}$, and the second produces a rotation of the projectile about its longitudinal axis (spinning motion) ω. There is no general requirement that the spin rate be coupled to the coning rate. However, the rotation about the longitudinal axis (p) can be forced to be zero in the nonrolling coordinate system by ensuring that ω be equal in magnitude but opposite in sign to the component of $\dot{\phi}$ along the longitudinal axis, $\omega = -\dot{\phi}\gamma$. The total angular velocity of the body about the longitudinal axis is then zero and the spin rate in the nonrolling coordinate system is zero: $p = 0$. Hence, the projectile angular motion is completely defined once the coning rate and the spin rate are specified.

The appeal of both of these methods is that only steady-state computations are required. In both methods, the motion can be decomposed into a combination of two orthogonal planar pitching motions. For steady lunar coning motion, there is no rotation of the pitch plane with respect to the body. The boundary conditions in the coning frame do not introduce any time dependency into the problem when observed from the coning reference frame, so that the resulting flowfield is expected to be steady for small angles of attack and small coning rates. Because the coning frame is rotating at a constant angular velocity and the body does not rotate with respect to the coning reference frame, there is no requirement of axisymmetry for steady flow to exist [4].

The case of steady combined spinning and coning motion is different, because the body will rotate in the coning reference frame at a rate that is proportional to the coning rate, $\omega = -\dot{\phi}\cos\alpha_t$. This rotation does not produce a time-dependent boundary condition for axisymmetric bodies, thus steady flow exists. However, for

Table 1 M910 computational mesh characteristics

Case	Number cells	Radial boundary, cal.	Front boundary, cal.	Rear boundary, cal.	First boundary-layer edge, cal.
RANS supersonic	1,952,480	3.51	0.31	5.31	1.54×10^{-5}
RANS subsonic	1,960,928	45.8	24.7	39.8	4.00×10^{-5}
RANS/LES supersonic	5,412,752	3.51	0.31	39.8	1.54×10^{-5}
RANS/LES subsonic	5,997,512	45.8	24.7	39.8	4.00×10^{-5}

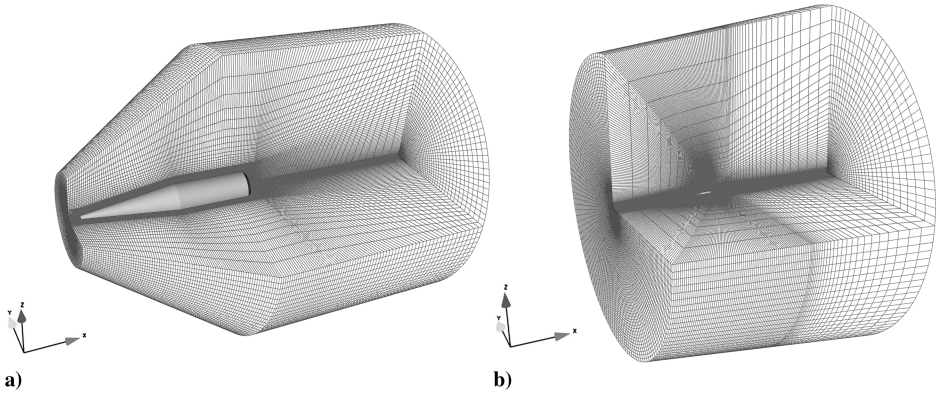

a) b)

Fig. 5 Computational mesh: a) supersonic case ($M > 1.4$) and b) sub/transonic cases ($M \leq 1.4$).

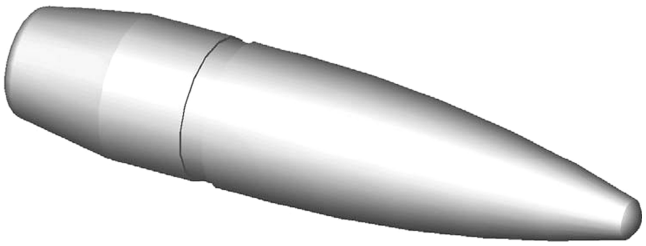

Fig. 6 Computational model: 0.50 cal..

nonaxisymmetric bodies, the rotation of the body in the coning reference frame will produce a time-dependent (periodic) boundary condition in the flow field, making the combined spinning and coning method appropriate only for axisymmetric bodies.

The detailed relationship between the side moment due to coning motion and the pitch-damping moment coefficient developed by Weinacht et al. [1] is summarized here. Note that the dynamic coefficients were nondimensionalized by $\dot{\phi}d/V$ in previous work [1–4], whereas here the convention of $\dot{\phi}d/2V$ is used. The moment formulation cast in terms of the in-plane and side moments is written as follows:

$$C_m + iC_n = C_{m_\alpha}\delta + i\left\{\left(\dot{\phi}\gamma d/2V\right)C_{n_{p\alpha}}\delta + \delta\left(\dot{\phi}d/2V\right)[C_{m_q} + \gamma C_{m_{\dot{\alpha}}}]\right\} \tag{1}$$

The in-plane moment (real part) results only from the pitching moment, whereas the total side moment (complex part) consists of contributions from the Magnus and the pitch-damping moments. For lunar coning motion, the side moment can be written as

$$C_n = \delta\left(\dot{\phi}d/2V\right)(\gamma C_{n_{p\alpha}} + [C_{m_q} + \gamma C_{m_{\dot{\alpha}}}]) \tag{2}$$

with the Magnus component due to the component of angular velocity along the longitudinal axis of the projectile. The right-hand side of Eq. (2) is simply the variation of side moment with coning rate,

$$C_{n_{\dot{\phi}}} \equiv [\partial C_n/\partial(\dot{\phi}d/2V)] = \delta[\gamma C_{n_{p\alpha}} + (C_{m_q} + \gamma C_{m_{\dot{\alpha}}})] \tag{3}$$

For bodies of revolution, a single computation at a nonzero coning rate is sufficient because the side moment for a projectile with zero coning rate is zero.

In the case of combined spinning and coning motion the spin rate of the projectile, as observed from the nonrolling coordinates, is zero. In the coning coordinate frame the body will spin in the opposite direction of the coning motion, that is, $\omega = -\dot{\phi}\gamma$, thereby canceling the induced spin rate due to coning motion. For this motion, the side moment can be written as

$$C_n = \delta\left(\dot{\phi}d/2V\right)[C_{m_q} + \gamma C_{m_{\dot{\alpha}}}] \tag{4}$$

In this case the side moment is directly proportional to the pitch-damping moment coefficient and no Magnus term appears in the equation. As noted by Weinacht et al. [1], even when using the combined spinning and coning motion and Eq. (4), the Magnus effect has not been entirely removed from the problem. For example, in the coning frame, the combination of angle of attack from the coning motion and spinning motion produce a Magnus-like effect that must be resolved by the CFD computations (i.e., the near-body mesh resolution must be adequate to resolve the boundary layer modification due to the Magnus effect). Many projectile and missile applications deal with small amplitude motions so that it is customary to linearize the equations of motion. In this case the cosine of the angle of attack, $\gamma \approx 1$, and the pitch-damping moment appears as $(C_{m_q} + C_{m_{\dot{\alpha}}})$.

B. Transient Planar Motion Methodology

A variety of approaches exist for processing the computed time-dependent force and moment data to extract the pitch-damping force and moment from the planar pitching motion [7–11]. In the current effort, the total normal force and pitching moment are assumed to have the functional dependence consistent with a linear force and moment expansion. When simplified for the case of planar pitching motion, the total pitching moment has the form shown in Eq. (5). A similar expansion exists for the normal force coefficient.

$$C_m = C_{m_\alpha}\sin\alpha + (C_{m_q} + C_{m_{\dot{\alpha}}})(\dot{\alpha}d/2V) \tag{5}$$

The angle of attack and angular rate are determined from the sinusoidal variation shown in Eq. (6).

$$\alpha = \alpha_0 \sin(\dot{\alpha}_0 t) \tag{6}$$

A least-squares fitting process is used to determine the two unknown coefficients, C_{m_α} and $(C_{m_q} + C_{m_{\dot{\alpha}}})$, using a series of predicted total pitching moments obtained at two or more independent angles and angular rates. Other methods [8–11] consider the first term in Eq. (5)

Table 2 Computational mesh characteristics: 0.50 cal.

Case	Number cells	Radial boundary, cal.	Front boundary, cal.	Rear boundary, cal.	First boundary-layer edge, cal.
Supersonic	5,905,658	5.3	5.8	14.9	1.9×10^{-5}
Subsonic	7,216,576	89.9	90.3	89.4	5.6×10^{-5}

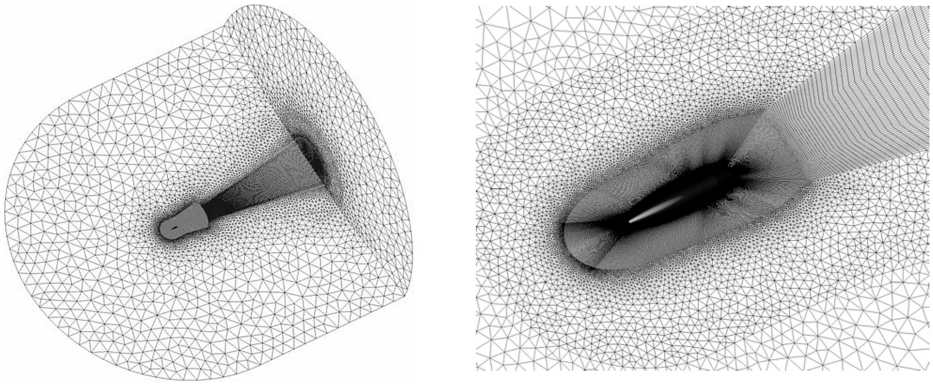

a) b)

Fig. 7 Typical computational meshes for 0.50-cal. projectile: a) subsonic mesh and b) close-up of supersonic mesh around which subsonic mesh was built.

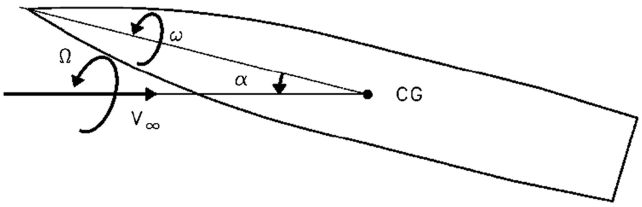

Fig. 8 Schematic of coning motion.

is known from the steady-state simulation and then calculate ($C_{m_q} + C_{m_{\dot{\alpha}}}$) directly. The same procedure is used to extract the normal force and pitch-damping force coefficients. For the results presented here, the normal force and pitching moment coefficients were well represented by the linear expansion once the initial transients, which occurred during the initiation of the planar pitching motion, damped out. Data from an entire cycle of motion were used to obtain the pitch-damping coefficients in the results presented here. Although it was determined that data from a portion of the yawing cycle were sufficient to accurately determine the pitch-damping coefficient, data from the full cycle of motion were obtained to ensure the assumed form properly represented the aerodynamic behavior across the range of angle of attack for the computation.

IV. Results and Discussion

A. Pitch-Damping Calculations

The CFD computations to calculate pitch-damping coefficients are separate from those used to calculate the other aeroballistic coefficients. The origin of the computational domain is moved to the projectile c.g. and then rotated in the pitch plane by the coning angle, typically 2 or 3-deg. For the pitch-damping computations, the computational domain is set to rotate about the x axis, which is no longer the projectile longitudinal axis, at the coning rate using a rotating-reference frame methodology to perform the steady-state computation. The steady state, rotating-reference frame methodology implemented in CFD++ limited the analysis to lunar coning, because a separate spinning boundary condition about an arbitrary axis could not be appropriately used in conjunction with the rotating-reference frame. The results shown in the following sections for the M910 and 0.50-cal. projectiles were all calculated using CFD++ and the steady-state lunar coning method. For the ANSR case, in addition to lunar coning predictions with CFD++, results are also shown for steady-state combined coning-spinning using OF 2 and a parabolized Navier–Stokes (PNS) code, and the transient planar pitching motion using OF-2.

Table 3 Comparison of corrected and uncorrected pitch-damping values for M910

Mach no.	$\lfloor C_{m_q} + C_{m_{\dot{\alpha}}} \rfloor$ (corrected)	$C_{n_{p\alpha}} + \lfloor C_{m_q} + C_{m_{\dot{\alpha}}} \rfloor$ [from Eq. (3)]	% difference
0.60	−6.34	−6.50	2.52
0.70	−5.59	−5.74	2.66
0.90	−9.17	−9.26	1.02
0.98	−11.99	−11.98	−0.05
1.02	−11.41	−11.42	0.05
1.20	−14.00	−13.87	−0.95
1.40	−13.74	−13.56	−1.32
2.00	−13.05	−12.87	−1.36
2.50	−12.22	−12.08	−1.14
3.50	−16.50	−16.40	−0.64
4.50	−15.66	−15.57	−0.56

The Magnus force and moment are small in relation to the pitch-damping coefficients and usually can be ignored when using the lunar coning motion. However, the computed Magnus moment coefficients are available from the steady-state computations of the projectile variation with angle of attack and Mach number. Those values of Magnus moment coefficient can be used in Eq. (3) to compute the pitch-damping coefficients. Although the induced spin rates due to lunar coning are much smaller than those used in the computations of Magnus moments, the Magnus moment coefficient was found in this and previous studies [1] to be relatively insensitive to spin rate. Table 3 shows a comparison of the corrected and uncorrected values of pitch-damping moment for the M910 projectile. The corrected values were obtained by subtracting the Magnus moment obtained during the static aerodynamic coefficient calculations (i.e., stationary reference frame, nonzero-angle of attack, and rotating surface boundary condition on projectile surface). The largest difference is about 2.6% at the lower Mach numbers, showing that neglecting the Magnus term does not incur a large error. However, the Magnus term is easily obtained from the other steady-state calculation and should be used to obtain the correct pitch-damping moment. Note that the issue of the accuracy of the steady-state computation of Magnus moment does not effect the correction to the pitch-damping term. The value calculated from the steady-state computation of Magnus moment is used because the coning motion is also a steady-state computation.

Before presenting the results for the three projectile configurations, several checks of the pitch-damping calculation via the steady lunar coning method are presented. Figure 9a shows the variation of the side moment due to coning with coning rate, Eq. (2), for two Mach numbers and three nondimensional coning rates, $\Omega d/2V =$ 0.0025, 0.005, and 0.010. The trend lines through the three data points show a very linear trend with a zero intercept, as it should be because Magnus effect is zero at zero spin rate. The slope of the side force curve is equal to the right-hand side of Eq. (3). The calculations using CFD++ in the following sections were performed with $\Omega d/2V = 0.005$ at a coning angle of 2 or 3-deg. The combined spinning and coning motion results using OF-2 and the PNS code

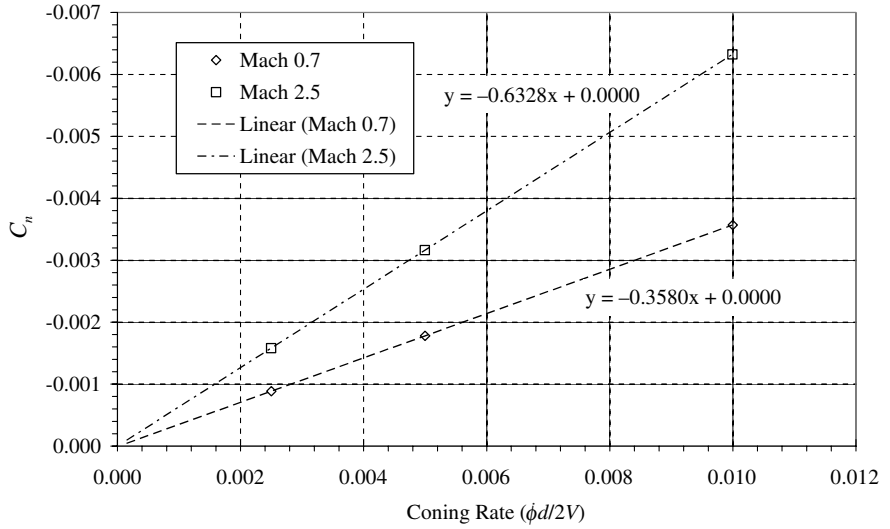

a)

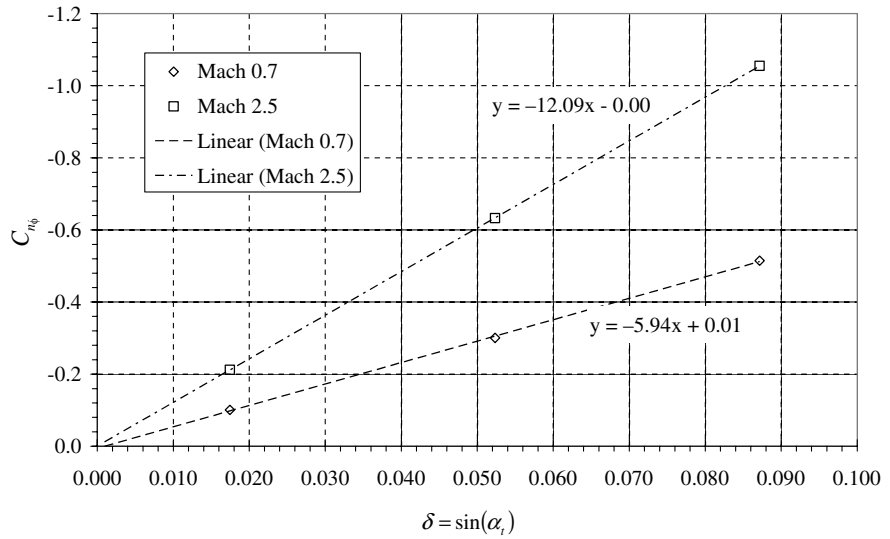

b)

Fig. 9 M910 projectile variation: a) side moment due to coning with coning rate, and b) side moment slope due to coning with angle of attack.

were obtained for coning angles of 2-deg and $\Omega d/2V = 0.0005$, 0.005, and 0.05. In general, there was little variation in the predicted pitch-damping moment coefficient across the coning rates examined.

Figure 9b shows the variation of this side moment slope with angle of attack for two Mach numbers and $\alpha = 1$, 3, and 5-deg. Again the variation is linear with zero intercept. The slope of this curve is equal to the right-hand side of Eq. (3) divided by δ, that is, the uncorrected pitch-damping moment. Therefore, the variation of predicted pitch-damping moment coefficient is also small across the coning angles investigated.

Although not presented in this paper, the pitch-damping force is also easily obtained from this method. Because Magnus and pitch-damping forces are rarely obtained from experimental methods, there was no comparison data to be shown. Obtaining these forces from the CFD is an added benefit of the computational method.

B. U.S. Army–Navy Spinner Rocket

A complete set of static and dynamic coefficients for the ANSR is reported elsewhere [19]. The roll damping moment, Magnus moment, and pitch damping moment are presented here in Figs. 10a–10c. Note that the experimentally determined dynamic derivatives generally have larger errors associated with them than the static coefficients, estimated at $\pm 20\%$ for Magnus and pitch damping, and $\pm 10\%$ for roll damping [32]. Error bars are not shown in the plots so that the clarity of the plots is not reduced.

The roll damping (Fig. 10a) compares reasonably well with the experimental data. The roll-damping values were obtained at $\alpha = 2$ deg. However, C_{lp} was found to be relatively insensitive to angle of attack up to the 5-deg level for each of the projectiles investigated in this study. Over the Mach number range shown, the CFD values of C_{lp} are under predicted (i.e., larger negative, so that damping is over predicted) by about 8–15%. The trend of decreasing roll damping with Mach number is predicted very well by the CFD.

Figure 10b shows the comparison of predicted and experimental Magnus moment for the middle c.g. location, 4.036 cal. The results for the other two c.g. locations followed the same trends. The predicted values fall within the data very well for $M \geq 1$. However, the experimental Magnus moment data shows a larger downward trend for $M < 1$ than the predicted values. Note there are extremely large amounts of scatter in the experimental data at all c.g. locations. Still, there is definitely a larger negative trend in the experimental data than there is in the CFD predictions. However, the ANSR does not exhibit the very large a negative Magnus moment indicative of nonlinear effects like the M910, shown in section IV.C, most likely due to the sharp-edged base.

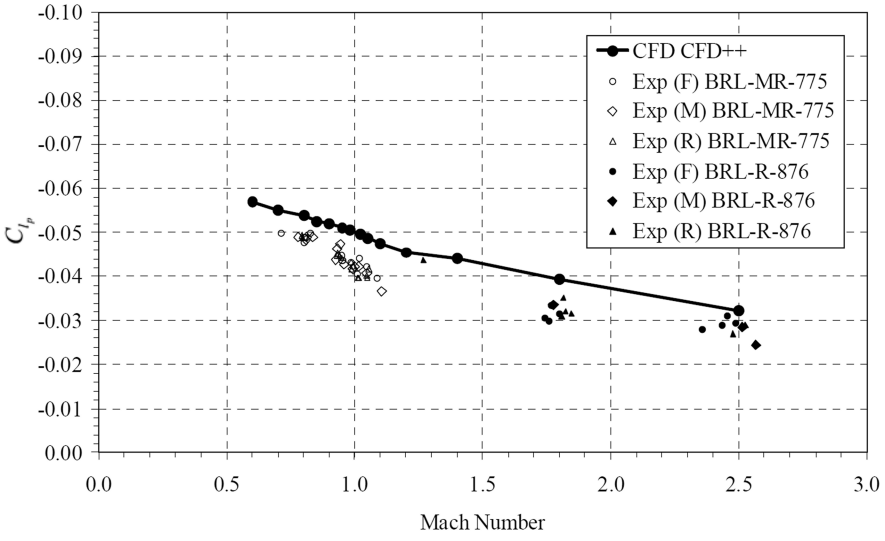

a)

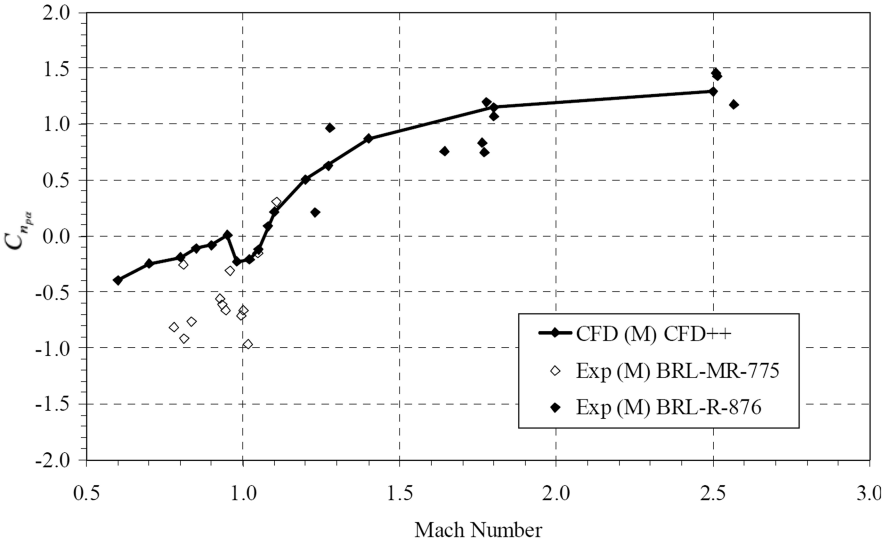

b)

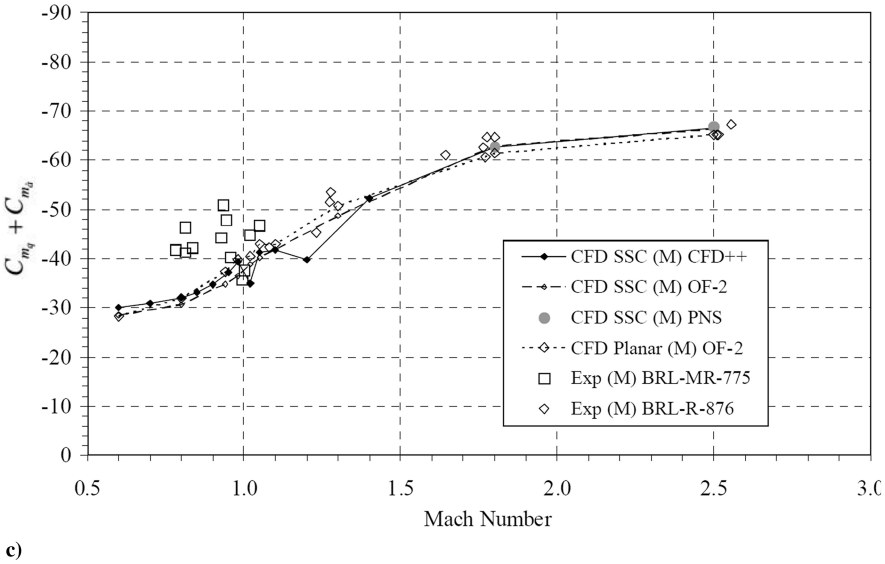

c)

Fig. 10 Aerodynamic coefficients, ANSR: a) roll damping, b) Magnus at $\alpha = 2$ deg, and c) pitch-damping moment sum.

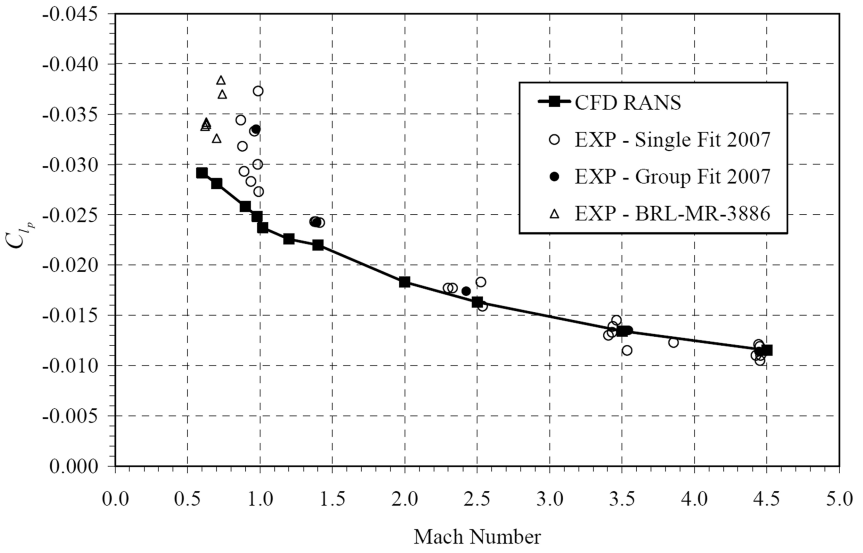

a)

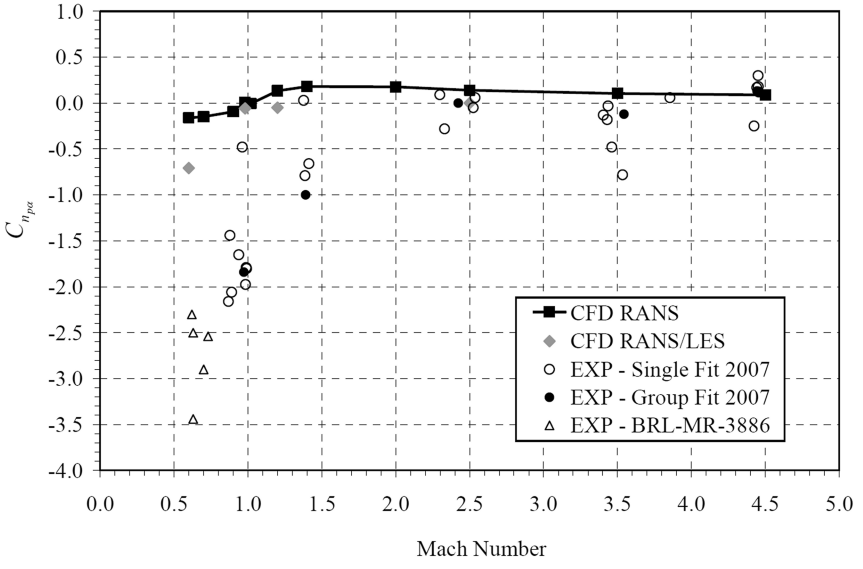

b)

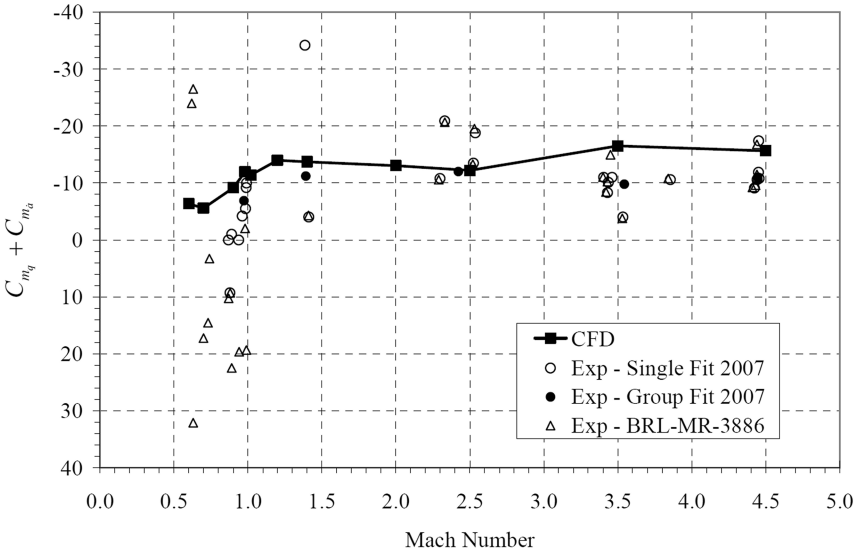

c)

Fig. 11 Aerodynamic coefficients, M910: a) roll damping, b) Magnus moment at $\alpha = 3$ deg, and c) pitch-damping moment sum.

Weinacht [33] demonstrated that the shape of the projectile base is likely the dominant cause of nonlinear Magnus moment; replacing a rounded base with a sharp, nearly square base nearly eliminated the nonlinear Magnus of a small-arms projectile. Whereas there is definitely more scatter in the experimental data at Mach numbers less than one, the variation of Magnus moment with angle of attack is still fairly linear [21,34].

Figure 10c shows the pitch-damping predictions for the middle c.g. location from three different CFD codes and two different methods: steady-state coning (SSC) using CFD++, SSC using OF-2, SSC using a PNS code [1] (supersonic Mach numbers only), and the transient, planar pitching motion using OF-2. Note, that the SSC CFD++ calculations were performed using the steady lunar coning motion; whereas the OF-2 and PNS SSC calculations were performed using the steady combined spinning and coning motion.

All four sets of CFD predictions compare to each other extremely well, adding a high degree of confidence to the predictions, despite differences in the codes and grids applied to obtain the results. The computed results also show good agreement with experimental data [21,34], particularly above the sonic velocity. Results at subsonic velocities show some degree of underprediction of the pitch damping, although there is significantly more scatter in the experimental data at these Mach numbers. Still, the CFD predictions fall within the error bounds, albeit at the ends of the error bounds at the lowest Mach numbers.

There are two features of the computed pitch-damping curves that differ between the CFD++ and OF-2 calculations. The CFD++ computations show a decrease in the absolute value of pitch damping of about 10–20% at Mach 1.02 and 1.2. The original level of pitch-damping is quickly recovered. The OF-2 coning computations show no decrease, but the number of data points in this region is lacking. The OF-2 planar pitching computations do show a small change in the value of pitch-damping at Mach 1.02 and 1.1. The fact that this effect is present in two very distinct simulation methods, both steady state and time accurate, and with different meshing methodologies, indicates that it may be real. It is likely that it is an effect of the shock interactions that occur in the transonic Mach number regime. The scatter in the experimental data makes it impossible to discern the trend.

C. M910: 25-Millimeter M910

The static aerodynamic coefficients, roll damping, and Magnus moments predicted using CFD++ were reported previously [18]. The roll damping and Magnus moments are shown in Fig. 11, along with the pitch-damping coefficient predictions. The predictions of roll damping (Fig. 11a) compare very well with the experimental data for $M > 1$. At and below Mach 1 the CFD predictions fall at the upper bound of the estimated error in the experimental values [18,35]. The CFD prediction is about 15% higher than the error bound of the group fit point [18] just below Mach 1. The C_{lp} values in Fig. 11 are for $\alpha = 3$ deg but the actual value was found insensitive to angle of attack.

The predictions of Magnus moment, Fig. 11b, again compare reasonably well in the supersonic region (in which the Magnus moment is very near zero). However, the CFD does not predict the large negative nonlinear Magnus moment at the lower Mach numbers. Time-accurate RANS/LES simulations better predicted the lower Magnus moment in the subsonic range, as shown in Fig. 11b. The magnitude of the Magnus moment did not approach that in the experimental data; however, this result is an indication that transient flow effects may have to be taken into account in the subsonic and transonic flight regimes to predict Magnus effects, at least for this projectile shape. The issue of Magnus prediction at lower Mach numbers is more fully addressed elsewhere [18,19].

The comparison of predicted and experimental pitch-damping moment coefficients is shown in Fig. 11c. The CFD predictions fall within the scatter in the experimental data across the Mach number range. The predicted pitch-damping coefficient again shows a dip in the absolute value at Mach 1.02, however, it is only about 4%. The comparison is very good for $M \geq 1$. At Mach numbers less than one, the experimental data (reduced using linear theory methods [35]) shows positive values of pitch-damping moment. When the more advanced 6-deg of freedom reductions were used to reduce the data (single and group fit 2007), the positive pitch-damping moment coefficient is eliminated, though in some cases by holding it fixed at zero. It is generally believed that the pitch-damping moment is not positive, and that small pitch-damping moment coefficients (absolute values less than 5) are difficult to resolve, especially when nonlinear Magnus moment coefficients are present. The values of cubic Magnus and pitch-damping moment coefficients are coupled and are difficult to separate even when the nonlinear least-squares data reduction process [36] is used. The question has been raised, and is currently under investigation, that if there are large errors associated with the experimental pitch damping, is the effect on the experimental Magnus moment truly known. One way that this discrepancy in the experimental data reductions has been overcome is to use multiple shots to determine a group fit and use this value fixed in the remainder of the experimental data reductions. The authors have a strong confidence in the CFD predicted values of pitch-damping moment at all Mach numbers. The accuracy of the Magnus predictions at the lower Mach numbers, especially via steady-state computations, is still at issue. However, we believe some of the experimental nonlinear Magnus data at the lower Mach numbers should also be questioned, especially if accompanied by positive pitch-damping values. The M910 provides a good configuration for the study of both nonlinear Magnus and pitch damping and further investigation is planned.

D. 0.50-Caliber Projectile

The CFD predictions of the roll damping, Magnus, and static aerodynamic coefficients for the 0.50-cal. projectile were previously reported [16]. The roll-damping and Magnus predictions are shown in Fig. 12 along with the prediction of the pitch-damping moment coefficients. The CFD predictions are compared with archival experimental data from the former U.S. Army Ballistic Research Laboratory (BRL) [30].

The 0.50 cal. is a body-engraved projectile. The CFD predictions do not include the engraving bands and were originally thought to be the likely reason for the lack of agreement with the experimental data [16]. However, recent investigations [37,38] on engraving of small-cal. rounds indicate that the engraving bands have little effect on the roll damping at the spin rates encountered in-flight and used in these studies. Further investigation into the previously reported discrepancies revealed that the experimental C_{lp} values reported in the data reduction were actually held fixed based on previous empirical estimates. The source of this empirical data is currently unknown. As the trend of the predicted C_{lp} is the same for the 0.50 cal. (Fig. 12a) as the experimental and computational results for the ANSR and M910 projectiles, the computational C_{lp} results for the 0.50-cal. projectile were then assumed correct.

Another set of experimental 0.50-cal. flight data that includes experimentally determined C_{lp} was recently brought to the attention of the authors and is included in Fig. 12a for comparison. The data is from the Defence Research and Development Canada (DRDC) Valcartier, and was provided to the authors with permission to publish under the auspices of the Technical Cooperation Program.[§] This data include results from two nominal Mach numbers, 1.5 and 2.4. The CFD compares quite favorably to the DRDC C_{lp} results at both Mach 1.5 and 2.4, indicating that the CFD values are reliable for $M \geq 1$. Unfortunately, no other experimental data were found for $M < 1$, but the trend of the CFD C_{lp} values in this range is in agreement with that observed for the ANSR and M910 projectiles.

The prediction of Magnus moment at $\alpha = 2$ deg is shown in Fig. 12b. In the supersonic regime, the experimental analyses show that Magnus moment remains approximately constant. The inclusion of the DRDC data shows a greater variation with Mach

[§]General information can be found at http://www.dtic.mil/ttcp/ [retrieved 28 May 2008].

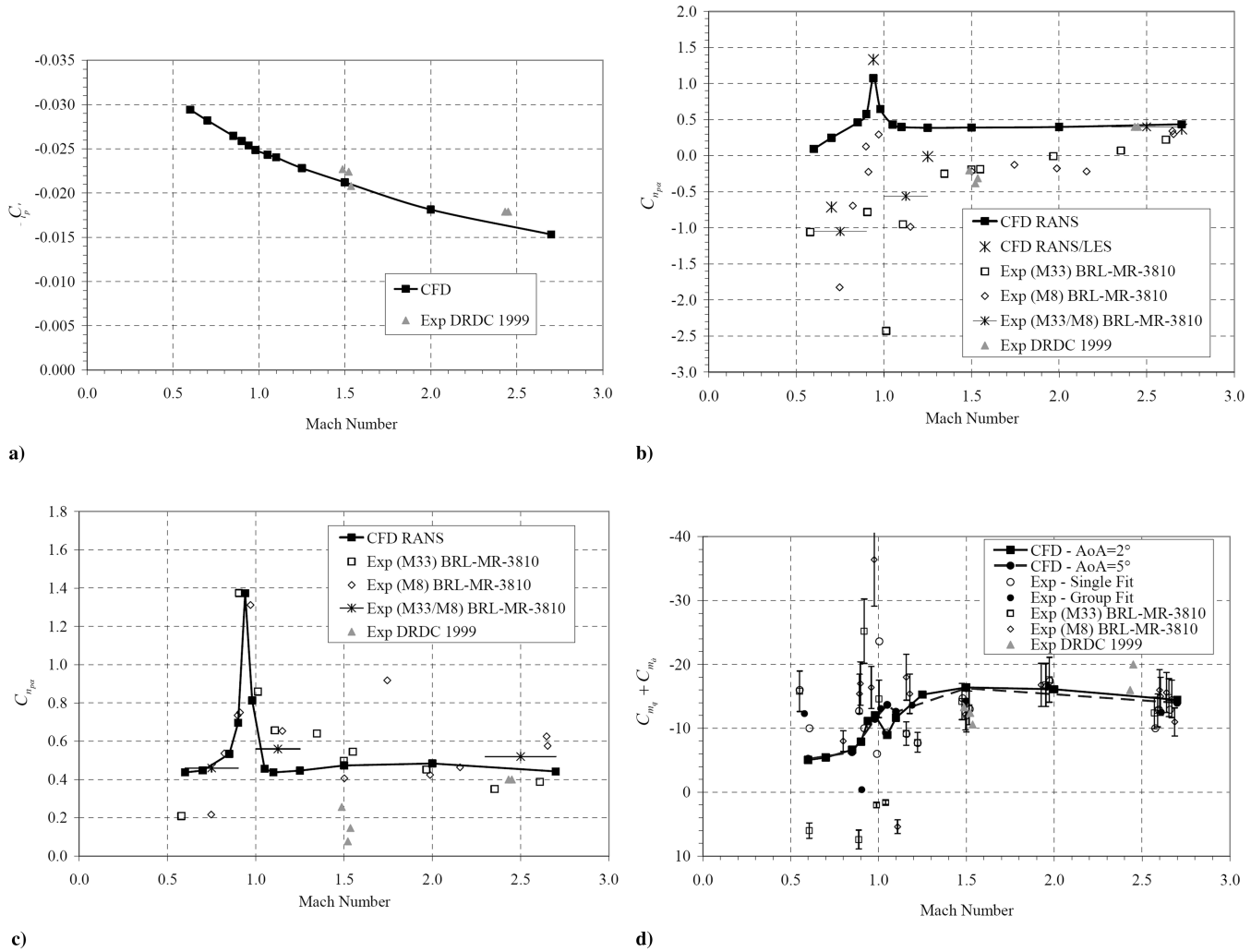

Fig. 12 Aerodynamic coefficients, 0.50-cal. projectile: a) roll damping, and b) Magnus moment at $\alpha = 2$ deg, c) Magnus at $\alpha = 5$ deg, and d) pitch-damping moment sum.

number than was originally found. However, at Mach 1.5, the transonic regime is being approached and greater nonlinearities may exist. The steady-state CFD predicts a nearly constant Magnus moment between Mach 1.1 and 2.7. The time-accurate, hybrid RANS/LES CFD produces nearly identical results to the steady-state CFD at Mach 2.7 but predicts a Magnus moment value closer to the experimental data at Mach 1.25. The hybrid RANS/LES CFD appears to be required at a significantly greater Mach number for the 0.50-cal. projectile than either the M910 or ANSR. The significant differences in the time accurate and steady-state results is also an indication that the boattail geometry with fillet is causing the flow to become unsteady at a much larger Mach number then a non-boattailed geometry. In the subsonic regime, the error in the experimental data is quite large, so that it is unclear as to what the trends actually are. However, the steady-state CFD over predicts the Magnus moment in this regime also. In the transonic regime, the general trend of a peak in Magnus moment is correctly predicted, but again the value is over predicted by the steady-state CFD. Silton [16] indicated that the discrepancy in the Magnus prediction might also be attributable to the lack of engraving in the CFD model. However, in computational and experimental investigations, respectively, Weinacht [37], and Silton and Webb [38] recently showed that engraving bands have little effect on the Magnus moment at the spin rates used in these studies. The time-accurate RANS/LES simulation predicts a value of Magnus moment that is considerably more in line with the experimental value (large negative number) indicating that Magnus moment is nonlinear in the subsonic regime. The transonic Mach number remains a bit of a mystery as the time-accurate RANS/LES simulations predicted a value quite near that of the steady-state simulation, which was unexpected. Other than the flow being highly nonlinear and transient near Mach 1, no explanation is available at this time.

At $\alpha = 5$ deg, the data trend in the steady-state CFD solution and experimental data appear to agree rather well (Fig. 12c). As such, no time-accurate solutions were completed at $\alpha = 5$ deg. The DRDC experimental data at Mach 2.4 is a little lower than the BRL experimental data (though approximately the same as the M33 data from the 6-degree-of freedom fits) and CFD predictions. The agreement of the CFD prediction with the experimental data in the supersonic regime is quite good, accurately predicting both trend and magnitude. The discrepancy between the BRL and DRDC data at Mach 1.5 indicate just how variable the Magnus moment can be. The CFD also accurately predicted the critical behavior in the transonic regime. However, as Mach 1 is approached, the CFD appears to under predict the Magnus moment, but is close to the error bound on the experimental data. The CFD again over predicts the Magnus moment in the subsonic regime.

Figure 12d shows the comparison of predicted pitch-damping moment with the experimental data. The DRDC and BRL experimental data generally agree to within the error bounds. The CFD predictions for coning angles of 2 and 5-deg are shown and they compare very well, differing only at one data point just above Mach 1. Interestingly, predicted values of pitch damping again show a dip in the absolute value just over Mach 1.0. For the 2-deg coning angle the reduction is about 22% at Mach 1.04, whereas for the 5-deg coning angle the reduction is about 8% at Mach 1.1. One

possibility is that there is a shock interaction effect responsible for the change in pitch damping near Mach 1.0. The predicted values generally fall within the experimental data for $M > 1$. Near Mach 1 and below the scatter in the experimental data is very large, including positive values of pitch-damping moment. The experimental data also exhibit some positive pitch-damping values in the range $0.6 < M < 1.0$. We believe the CFD predicted values may once again be assumed to be the more reliable values for $M < 1$.

V. Conclusions

The prediction of the dynamic stability derivatives, roll damping, Magnus, and pitch-damping moments were presented for three spin-stabilized projectiles. Roll damping was shown to be adequately predicted via steady-state CFD methods. The prediction of Magnus moment in the supersonic flight regime was also shown to be adequate using steady-state methods. However, in the subsonic and transonic flight regime the accuracy of CFD prediction of Magnus moment is not clearly defined. The CFD usually predicted the decreasing trend of Magnus moment with decreasing Mach number; however, the steady-state CFD over predicted the value of Magnus moment at the lower Mach numbers. Time-accurate RANS/LES simulations improved the CFD predictions of Magnus moment for the M910 projectile but had little effect on the Magnus moment predicted for the ANSR. The prediction of Magnus issue is still under investigation.

A primary focus of the present paper was the demonstration of the capability to predict the pitch-damping moment via steady-state CFD methods. The pitch-damping moment predicted by the CFD compared very well with available experimental data for the three projectiles investigated. The only discrepancy was at the lower Mach numbers, in which the experimental data showed a large level of scatter and was sometimes accompanied by unlikely positive values of pitch-damping moment. Therefore, the CFD prediction should be assumed the more accurate value at the lower Mach numbers.

The prediction of pitch-damping of the ANSR was demonstrated by several CFD codes, two different steady-state CFD methods, and a time-accurate planar pitching motion method. All methods compared extremely well with each other and to the experimental data.

Roll-damping and pitch-damping CFD predictions were found to be very good across the Mach number ranges investigated. The limitations of small angle of attack and low spin rates for the pitch-damping calculations do not hinder the usefulness of the method because they are adequate for most cases. The accuracy of the Magnus moment predictions was very good in the supersonic flight regime but varied in the sub- and transonic flight regimes. The best comparison of Magnus moment prediction with experimental data was found for the nonboattailed, ANSR configurations, which did not have highly nonlinear Magnus moments. These results demonstrate that steady-state CFD methods can be adequate to predict the dynamic derivatives of spin-stabilized projectiles. Time-accurate methods need be resorted to include only those cases necessary, making the most efficient use of computational resources.

Acknowledgments

The authors thank Daniel Corriveau of the DRDC Valcartier, for supplying additional 0.50-cal. aeroballistic range test data and obtaining permission for us to publish. This work was supported in part by a grant of high-performance computing time from the U.S. Department of Defense High Performance Computing Modernization Program at the U.S. ARL Major Shared Resource Center, Aberdeen Proving Ground, Maryland.

References

[1] Weinacht, P., Sturek, W. B., and Schiff, L. B., "Navier–Stokes Predictions of Pitch Damping for Axisymmetric Projectiles," *Journal of Spacecraft and Rockets*, Vol. 34, No. 6, 1997, pp. 753–761. doi:10.2514/2.3306

[2] Weinacht, P., "Navier–Stokes Predictions of the Individual Components of the Pitch-Damping Sum," *Journal of Spacecraft and Rockets*, Vol. 35, No. 5, 1998, pp. 598–605. doi:10.2514/2.3390

[3] Weinacht, P., "Prediction of Pitch-Damping of Projectiles at Low Supersonic and Transonic Velocities," AIAA, Paper 98-0395, Jan. 1998.

[4] Weinacht, P., and Sturek, W. B., "Navier–Stokes Predictions of Pitch Damping of Finned Projectiles Using Steady Coning Motion," AIAA, Paper 90-3088, Aug. 1990.

[5] Sturek, W. B., Nietubicz, C. J., Sahu, J., and Weinacht, "Applications of Computational Fluid Dynamics to the Aerodynamics of Army Projectiles," *Journal of Spacecraft and Rockets*, Vol. 31, No. 2, 1994, pp. 186–199. doi:10.2514/3.26422

[6] Weinacht, P., "Projectile Performance, Stability, and Free-Flight Motion Prediction Using Computational Fluid Dynamics," *Journal of Spacecraft and Rockets*, Vol. 41, No. 2, 2004, pp. 257–263. doi:10.2514/1.1037

[7] Park, S. H., Kim, Y., and Kwon, J. H., "Prediction of Damping Coefficients Using the Unsteady Euler Equations," *Journal of Spacecraft and Rockets*, Vol. 40, No. 3, 2003, pp. 356–362; doi:10.2514/2.3970; also AIAA 2002-0715, Jan. 2002.

[8] Park, S. H., and Kwon, J. H., "Navier–Stokes Computations of Stability Derivatives for Symmetric Projectiles," AIAA, Paper 2004-0014, Jan. 2004.

[9] Oktay, E., and Akay, H. U., "CFD Predictions of Dynamic Derivatives for Missiles," AIAA 2002-0276, Jan. 2002;

[10] Stalnaker, J. F., and Robinson, M. A., "Computations of Stability Derivatives of Spinning Missiles Using Unstructured Cartesian Meshes," AIAA, Paper 2002-2802, June 2002.

[11] Sahu, J., "Numerical Computations of Dynamic Derivatives of a Finned Projectile Using a Time-Accurate CFD Method," AIAA, Paper 2007-6581, Aug. 2007.

[12] Sahu, J., "Time-Accurate Computations of Free-Flight Aerodynamics of a Spinning Projectile with Flow Control," AIAA, Paper 2006-6006, Aug. 2006.

[13] Sturek, W. B., and Schiff, L. B., "Computations of the Magnus Effect for Slender Bodies in Supersonic Flow," *AIAA Journal*, Vol. 20, No. 12, 1982, pp. 1724–1731. doi:10.2514/3.8011

[14] Nietubicz, C. J., Sturek, W. B., and Heavey, K. R., "Computations of Projectile Magnus Effect at Transonic Velocities," U.S. Army Ballistic Research Laboratory, BRL-TR-02515, Aberdeen Proving Ground, MD, Aug. 1983.

[15] Sahu, J., "Transonic Navier–Stokes Computations for a Spinning Body of Revolution," U.S. Army Ballistic Research Laboratory, BRL-TR-3265, Aberdeen Proving Ground, MD, Sept. 1991.

[16] Silton, S. I., "Navier–Stokes Computations for a Spinning Projectile from Subsonic to Supersonic Speeds," *Journal of Spacecraft and Rockets*, Vol. 42, No. 2, 2005, pp. 223–231; doi:10.2514/1.4175; also AIAA 2003-3936, June 2003.

[17] DeSpirito, J., and Heavey, K. R., "CFD Computation of Magnus Moment and Roll Damping Moment of a Spinning Projectile," AIAA, Paper 2004-4713, Aug. 2004.

[18] DeSpirito, J., and Plostins, P., "CFD Prediction of M910 Projectile Aerodynamics: Unsteady Wake Effect on Magnus Moment," AIAA, Paper 2007-6580, Aug. 2007.

[19] DeSpirito, J., "CFD Prediction of Magnus Effect in Subsonic to Supersonic Flight," AIAA, Paper 2008-0427, Jan. 2008.

[20] "FLUENT 6.3 User's Guide," Vol. 2, Fluent, Inc., Lebanon, NH, Sept. 2006.

[21] Schmidt, L. E., and Murphy, C. H., "The Aerodynamic Properties of the 7-Caliber Army-Navy Spinner Rocket in Transonic Flight," U.S. Army Ballistics Research Laboratory, BRL-MR-775, Aberdeen Proving Ground, MD, March 1954.

[22] "CFD++ User's Manual," Metacomp Technologies, Inc., Agoura Hills, CA, 2006.

[23] Renze, K. J., Buning, P. G., and Ragagopalan, R. G., "A Comparative Study of Turbulence Models for Overset Grids," AIAA, Paper 92-0437, Jan. 1992.

[24] Meakin, R. L., "A New Method for Establishing Inter-grid Communication Among Systems of Overset Grids," AIAA, Paper 91-1586, June 1991.

[25] Chan, W. M., "The Overgrid Interface for Computational Simulations on Overset Grids," AIAA, Paper 2002-3188, June 2002.

[26] Baldwin, B. S., and Barth, T. J., "A One-Equation Turbulence Transport Model, for High Reynolds Number Wall-Bounded Flows," AIAA, Paper 91-610, Jan. 1991.

[27] Park, S. H., and Kwon, J. H., "Navier–Stokes Computation of Pitch-

Damping Coefficients Using Steady Coning Motion," *Journal of Spacecraft and Rockets*, Vol. 41, No. 5, 2004, pp. 754–761; doi:10.2514/1.2024; also AIAA Paper 2003-3671, June 2003.

[28] Murman, S. M., Chan, W. M., Aftosmis, M. J., and Meakin, R. L., "An Interface for Specifying Rigid-Body Motions for CFD Applications," AIAA, Paper 2003-1237, Jan. 2003.

[29] Chan, W. M., and Buning, P. G., "User's Manual for FOMOCO Utilities–Force and Moment Computation Tools for Overset Grids," NASA TM-110408, July 1996.

[30] McCoy, R. L., "The Aerodynamic Characteristics of .50 Ball, M33, API, M8, and APIT, M20 Ammunition," U.S. Army Ballistic Research Laboratory BRL-MR-3810, Aberdeen Proving Ground, MD, Jan. 1990.

[31] "GRIDGEN Users Manual," Pointwise, Inc., Bedford, TX, 2006.

[32] "ARFDAS 4.11 User's Guide," Arrow Tech Associates, South Burlington, VT, 1997.

[33] Weinacht, P., "Characterization of Small-Caliber Ammunition Performance Using a Virtual Wind Tunnel Approach," AIAA, Paper 2007-6579, Aug. 2007.

[34] Murphy, C. H., and Schmidt, L. E., "The Effect of Length on the Aerodynamic Characteristics of Bodies of Revolution in Supersonic Flight," U.S. Army Ballistics Research Laboratory BRL-R-876, Aberdeen Proving Ground, MD, Aug. 1953.

[35] Plostins, P., McCoy, R. L., and Wagoner, B. A., "Aeroballistic Performance of the 25 mm M910 TPDS-T Range Limited Training Projectile," U.S. Army Ballistic Research Laboratory, BRL-MR-3886, Aberdeen Proving Ground, MD, Jan. 1991.

[36] McCoy, R. L., *Modern Exterior Ballistics: The Launch and Flight Dynamics of Symmetric Projectiles*, Schiffer Publishing, Atglen, PA, 1998, pp. 273–298.

[37] Weinacht, P., "Validation and Prediction of the Effect of Rifling Grooves on Small-Caliber Ammunition Performance," AIAA, Paper 2006-6010, Aug. 2006.

[38] Silton, S., and Webb, D., "Experimental Determination of the Effect of Rifling Grooves on the Aerodynamics of Small Caliber Projectiles," AIAA, Paper 2006-6009, Aug. 2006.

M. Costello
Associate Editor